IEEE Access
Multidisciplinary ⁝ Rapid Review ⁝ Open Access Journal

Received April 12, 2021, accepted May 3, 2021, date of publication May 7, 2021, date of current version June 4, 2021.

Digital Object Identifier 10.1109/ACCESS.2021.3078338

Comparative Study of E- and U-core Modular Dual-Stator Axial-Field Flux-Switching Permanent Magnet Motors With Different Stator/Rotor-Pole Combinations Based on Flux Modulation Principle

SHUAI WANG[1], KEMAN LIN[2], (Member, IEEE), MINGYAO LIN[1], (Member, IEEE), YONG KONG[1], DA XU[3], NIAN LI[3], AND PENG WANG[1]
[1]School of Electrical Engineering, Southeast University, Nanjing 210000, China
[2]College of Energy and Electrical Engineering, Hohai University, Nanjing 210000, China
[3]School of Automation, Nanjing University of Science and Technology, Nanjing 210000, China

Corresponding author: Mingyao Lin (mylin@seu.edu.cn)

This work was supported in part by China NCFC under Grant 51937002, and in part by the Scientific Research Foundation of Graduate School of Southeast University, under Grant YBPY1973.

ABSTRACT In this paper, the dual-stator axial-field flux-switching permanent magnet (DSAFFSPM) motors with E- and U-core stator modular segments, as well as different stator/rotor-pole combinations are compared. The operation performance of the DSAFFSPM machines are explored by using the MMF-permeance model method. A more comprehensive theoretical analysis, no more limited to numerical calculation, is presented. This reveals directly the relations between the operation performance and design parameters of the machine. The performance comparisons between the E-shaped and U-shaped teeth DSAFFSPM machines are given, including the effects of the structural parameters on the electromagnetic torque, different stator/rotor-pole combinations on the winding factor and gear ratio, the differences of the average torque and the torque density and the efficiency in the 12/10 U-core and 6/10 E-core topology. These are the basis of the DSAFFSPM machine design and optimization. Finally, the experiments on the two prototype, 6/10 E-core and 12/10 U-core DSAFFSPM machines are carried out. The results show that the average torque of the 12/10 U-core prototype is higher than that of the 6/10 E-core prototype, while the torque density and the efficiency of 6/10 E-core DSAFFSPM machines are much higher.

INDEX TERMS Dual-stator axial-field flux-switching permanent magnet (DSAFFSPM), E-core and U-core, flux modulation principle, magnetomotive force (MMF)-permeance-model.

I. INTRODUCTION

With the merits of high torque density and high efficiency, the permanent magnet (PM) machines have attracted much more attention and thus have been widely used in industrial applications, including the servo systems, direct-drive systems and wind power generations [1]–[5], etc. Since PMs of conventional PM machines are always aligned in the rotor, the eddy current loss of the permanent magnet will cause the rotor heat difficult to dissipate, thus affecting the performance of the motor. A growing number of scholars have made great efforts on a new topology in which the PMs are located in the stator instead of the rotor. Among those stator-PM machines, namely flux-reversal PM machines (FRPM) [6], flux-switching PM machines (FSPM) and double salient PM (DSPM) machines [7], the FSPM machines have been of great interest these years.

The FSPM machine was first proposed in 1995 [8]. In [9]–[12], the comparison of FSPM machines and convention PM motors were presented in details and FSPM machines have more sinusoidal back-EMF and thus smaller torque ripple. Most studies on FSPM machines have been concentrated on proposing new topologies [13]–[18]. According to the direction of the magnetic flux circuit, it could be divided into radial flux type [13], axial flux type [14], [16], [17] and linear type [15]. Then, based on the number of stator and rotor, it can be classified by: dual-rotors-single-stator [16] and dual-stators-single-rotor [17]. Further, these researches can

The associate editor coordinating the review of this manuscript and approving it for publication was Yi Liu.

be grouped by: 1) different stator topologies, i.e., E-core and U-core stator modules [14], [15], [27]; 2) different winding configurations, i.e., concentrated winding, distributed winding and toroidal winding [18]; 3) different PM magnetization directions, i.e., adjacent PMs with same and with opposite magnetizing direction. What's more, some theoretical analysis on the electromagnetic performance of FSPM have been presented, such as MMF-permeance-model method [13], permeance and inductance modeling [19], magnetic circuit modeling [20], non-linear analytical modelling [21], doubly-salient relative permeance method [22].

Among the AFFSPM machines, double-stator or double-rotor axial-field flux-switching PM motors are widely studied due to their compact structure, small size, stable operation, great thermal management, high torque density and high efficiency [16], [23], [24], which is especially suitable for the wheel hub drive. However, it is easy to find from the previous literatures that although the axial structure has been used in the previous literature, the description of the axial flux switching motor was more limited to numerical analysis. A more comprehensive analysis is needed for the axial flux switching motor. The influence of different stator modules, i.e., E-core and U-core has just been given by simulation analysis while not validated theoretically by establishing an explicit mathematical model as well. In the meanwhile, the characteristics of DSAFFSPM machines with different stator/rotor-pole combinations have not been quantified with detailed parameters, such as the winding factor and the gear ratio.

In this paper, with the purpose of obtaining the optimal design parameters, DSAFFSPM machines with different modular stator topologies such as E-core and U-core with concentrated tooth-coil windings are analyzed based on the flux modulation principle, using the air-gap MMF-permeance model. In section II, the unified MMF-permeance model considering different modular stators of the machine is introduced. The principle of airgap flux density distribution, the working harmonics and the influence of stator core type of DSAFFSPM machines are revealed with analytical expressions. In section III, the influence of E-core and U-core modular stators on air-gap field harmonics is investigated, together with different modular stator design parameters and different stator/rotor pole-number combinations. In addition, the contribution of working harmonics to flux density, EMF and electromagnetic torque is analyzed, taking advantage of FEA. In section IV, two topologies, i.e.,12/10 U-core and 6/10 E-core DSAFFSPM machines are built and measured in order to verify the FEA results and the above analysis based on the flux modulation.

II. TOPOLOGY AND MODULATION PRINCIPLE

The basic structure of DSAFFSPM machines with concentrated tooth-wound windings and U-core/E-core stator modules are presented in Fig. 1(a) and Fig. 1(b), respectively.

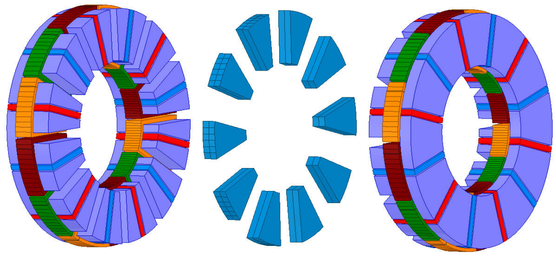

(a)

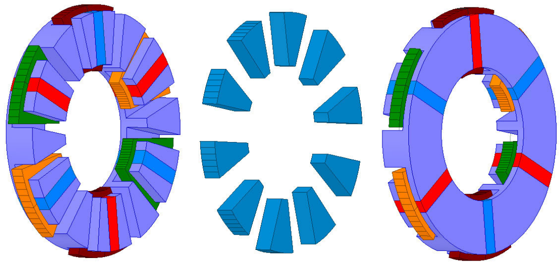

(b)

FIGURE 1. Configurations of two DSAFFSPM machines. (a) 12/10 U-core. (b) 6/10 E-core.

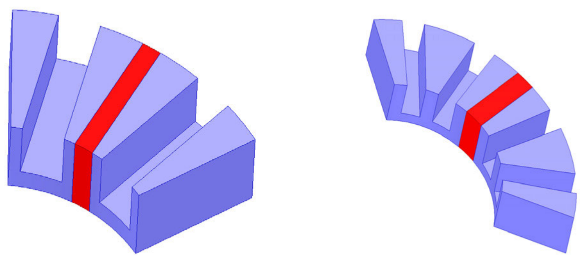

FIGURE 2. Configurations of two different stator modules. (a) U-core. (b) E-core.

They contain three parts, namely dual stators and one rotor sandwiched in between. The stator is constituted by the several identical modules, which can be seen in Fig. 2. Stator-side PMs are all circumferentially magnetized in the opposite direction, and circumferentially aligned between adjacent modules. It can be observed that the rotor has salient poles and the rotor-PMs are removed.

The stator-side PMs provide a stationary PM MMF, which is modulated by the uneven permeance distribution of the rotatory salient poles. Then, the stationary MMF can be modulated into an air-gap magnetic field composed of abundant harmonics based on the flux modulation principle. To investigate the field flux modulation effect of DSAFFSPM machines, the MMF-permeance model considering the uneven air-gap permeance distribution due to the rotor slotting is utilized. In the following analysis, p_m, p_r, p_a represent the pole-pair-number of PMs, rotors and armature windings, respectively.

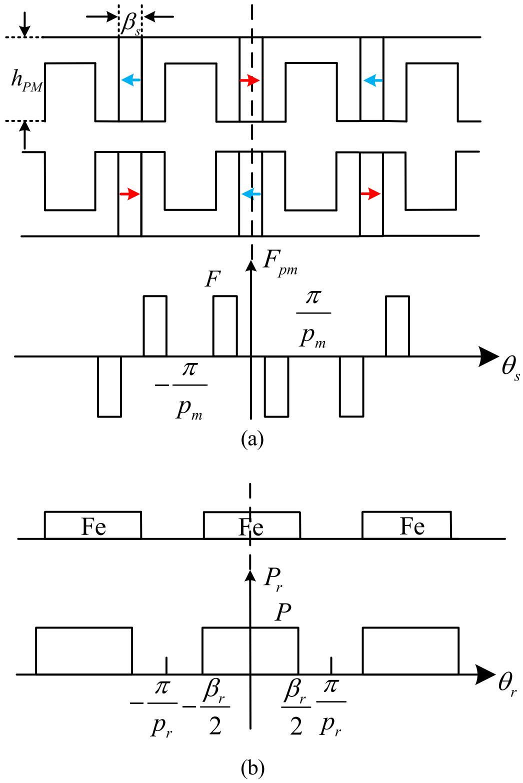

FIGURE 3. Diagram and MMF-permeance model of stator and rotor. (a) Stator diagram and corresponding PM MMF. (b) rotor diagram and corresponding permeance.

A. NO-LOAD AIR-GAP FLUX DENSITY

It can be seen, Fig.3(a) shows the air-gap PM MMF generated by stator-side PMs, whilst Fig.3(b) illustrates the air-gap permeance model accounting for rotor iron pieces, respectively. Since the MMF-permeance model has been proven to be valid, the no-load air-gap flux density can be deduced by multiplying $F_{pm}(\theta_s)$ and $P_r(\theta_s, t)$ as [25]

$$B(\theta_s, t) = F_{pm}(\theta_s) \times P_r(\theta_s, t) \tag{1}$$

where $F_{pm}(\theta_s)$ is the PM MMF, $P_r(\theta_s, t)$ is the specific air-gap permeance function. The first term in (1) is static while the latter one is rotary under the same stator reference frame, θ_s is the angle along the stator circumference.

The stationary PM MMF can be derived according to Fig. 2(a) in Fourier series as (2):

$$\begin{aligned} F_{PM}(\theta_s) &= \sum_{i=1,3,5}^{\infty} F_i \sin(ip_m\theta_s) \\ F_i &= \frac{8F}{\pi i} \sin(ip_m\frac{\beta_s}{2}) \sin(ip_m\frac{\theta_s}{2}) \\ F &= \frac{B_r h_{pm}}{\mu_r \mu_0} \end{aligned} \tag{2}$$

where i is the order of Fourier Series, F_i denotes the Fourier coefficient of $F_{PM}(\theta_s)$ waveform related to i, F is the amplitude of PM MMF, β_s refers to the width of PMs, θ_s indicates the sum of the width of PM and stator tooth, B_r, h_{pm}, μ_r are the remanence, the height and the relative permeability of PMs respectively.

The air-gap permeance function $P_r(\theta_s, t)$ is a relatively complex function about the shape of stator and rotor. In this paper, $P_r(\theta_s, t)$ is calculated without considering the slot shape and displayed as the configuration of Fig. 3(b). $P_r(\theta_s, t)$ in accordance with Fig. 3(b) could be expressed in Fourier series as (3):

$$P_r(\theta_s, t) = \sum_{k=0,1,2}^{\infty} P_k \cos kp_r\theta_r = \sum_{k=0,1,2}^{\infty} P_k \cos(kp_r\theta_s - p_r\omega t) \tag{3}$$

where k is the order of Fourier Series, P_k denotes the Fourier coefficient of $P_r(\theta_s, t)$ waveform connected with k and ω is the angular speed of the rotor.

Substituting (2)-(3) into (1), the no-load air-gap flux density $B(\theta_s, t)$ can expressed as below.

$$B(\theta_s, t) = \frac{1}{2} \sum_{k=0,1,2}^{\infty} \sum_{i=1,3,5}^{\infty} F_i P_k \sin[(ip_m \pm kp_r)\theta_s \mp p_r\omega t] \tag{4}$$

As shown in (4), $(ip_m \pm kp_r)th$ flux density harmonics are generated owing to the modulation of the stator-side PM MMF and rotating rotor iron pieces. The order of DSAFFSPM machines' working harmonics are extended from only p_r pole-pair to $(ip_m \pm kp_r)$ pole-pair, and the higher utilization of PMs can be obtained. These predicted filed harmonics can be classified into two types, 1) stationary, 2) rotating. When $k = 0$, only p_m pole-pair stationary harmonic flux density exists because PMs are mounted in the stator. On the other hand, when $k \neq 0$, the $(ip_m \pm kp_r)th$ rotatory flux density is induced due to the flux modulation of rotor iron pieces.

B. BACK-EMF AND TORQUE

Different from those rotor-side PM-excited machines such as the magnetic gear machine and the vernier machine, the analytical expression of flux density of DSAFFSPM machines is much less affected by the stator profile since the PM MMF is modulated mostly by rotor salient iron pieces [26]. However, when it comes to the back-EMF and the electromagnetic torque, the different stator modular profiles could be of critical impact. The influence and its theoretical derivation of E-core and U-core stator modular will be explained as follows.

1) U-CORE

Given that the permeance P_0 and P_1 have a much larger magnitude than the other order of air-gap permeance [27], the high-order permeance harmonics are neglected and the air-gap permeance function $P_r(\theta_s, t)$ can be rewritten as (5):

$$\begin{aligned} P_r(\theta_s, t) &= P_0 + P_1 \cos(p_r\theta_s - p_r\omega t) \\ P_0 &= \frac{P}{2\pi} p_r \beta_r, \quad P_1 = \frac{2P}{\pi} \sin p_r \frac{\beta_r}{2} \end{aligned} \tag{5}$$

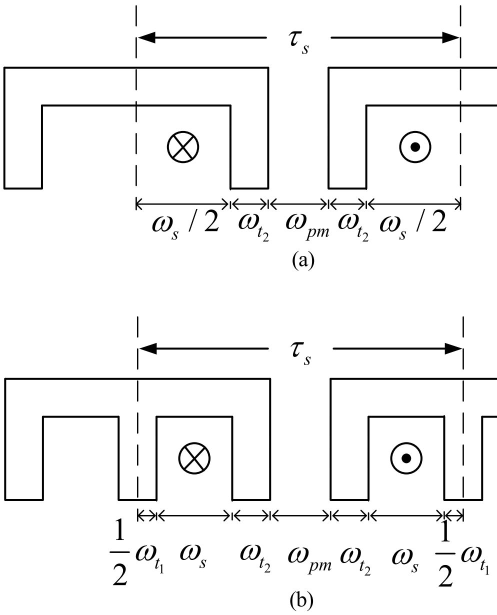

FIGURE 4. Cross sections of two different stator modules with schematic dimensions. (a) U-core. (b) E-core.

where P is the amplitude of the air-gap permeance and β_r is the width of a rotor iron piece.

Substituting (2) and (5) into (1), the no-load air-gap flux density can be represented as (6):

$$B(\theta_s, t) = \sum_{i=1,3,5}^{\infty} F_i \sin(ip_m\theta_s) \times P_0 + \frac{1}{2}\sum_{i=1,3,5}^{\infty} F_i P_1 \sin[(ip_m \pm p_r)\theta_s \mp p_r\omega t] \tag{6}$$

Benefiting from the stator modular structure and the concentrated tooth-coil, the simple superposition of $B(\theta_s, t)$ can be adopted, instead of the winding function, to calculate flux through coil A. Since $ip_m \pm p_r$th flux density harmonics are generation by the modulation of rotor poles, just define $p_{mo} = ip_m \pm p_r$. According to Fig.4(a), the flux through coil A is displayed as (7), as shown at the bottom of the next page: where n_{pc} denotes the number of turns per coil, l_{stk} shows the active length, r_{si} is the diameter of the air gap, θ_0 indicates the initial position of the stator, ω_{pm} is the width between adjacent two stator modules in which PMs are placed, ω_s and ω_t represent the width of the stator slot and teeth, respectively, and τ_s is the stator pole pitch.

Thus, the induced back-EMF in coil A can be derived as (8):

$$\begin{aligned} E_A &= -\frac{d\varphi_A}{dt} \\ &= \sum_{i=1,3,5}^{\infty} K_{Ai} \cos\frac{(ip_m \pm p_r)(\theta_{cons} \mp 2p_r\omega t)}{2} \\ K_{\mathrm{Ai}} &= \mp 4 n_{pc} l_{stk} r_{si} F_i P_1 p_r \omega \omega_{ts} \omega_{pms} \\ \theta_{cons} &= 2\theta_0 + \omega_s + \omega_{pm} + \omega_t \\ \omega_{ts} &= \cos(ip_m \pm p_r)\omega_t \\ \omega_{pms} &= \cos(ip_m \pm p_r)\frac{\omega_{pm}}{2} \end{aligned} \tag{8}$$

It is found that the fundamental PM MMF F_1 has much higher magnitude than other orders of PM MMF harmonics, and contributes mostly to the back-EMF, so the other order harmonics can be neglected and the back-EMF can be rewritten as (9):

$$\begin{aligned} E_A &= -\frac{d\varphi_A}{dt} \\ &= K_A \cos\frac{p_{mo}(2\theta_0 + \omega_s + \omega_{pm} + \omega_t \mp 2p_r\omega t)}{2} \\ K_{\mathrm{A}} &= \mp 4 n_{pc} l_{stk} r_{si} F_1 P_1 p_r \omega \cos(p_{mo}\omega_t) \cos p_{mo}\frac{\omega_{pm}}{2} \end{aligned} \tag{9}$$

Considering the machine current is of sinusoidal wave, the average torque can be obtained as (10):

$$\begin{aligned} T_e &= \frac{3}{2} n_{ph} k_w I_A E_A \\ &= K_T \cos\frac{p_{mo}(\theta_{cons} \mp 2p_r\omega t)}{2} \\ K_T &= 6 n_{ph} n_{pc} k_w I_A l_{stk} r_{si} F_1 P_1 p_r \omega \omega_{ts} \omega_{pms} \\ \theta_{cons} &= 2\theta_0 + \omega_s + \omega_{pm} + \omega_t \\ \omega_{ts} &= \cos p_{mo}\omega_t \\ \omega_{pms} &= \cos p_{mo}\frac{\omega_{pm}}{2} \end{aligned} \tag{10}$$

where n_{ph} denotes the number of series turns per phase and k_w indicates the winding factor of the armature related to the configuration of windings.

2) E-CORE

Because of the same rotor topology, it does not make sense for the analytical expression of no-load airgap flux density whether E-core and U-core stator modules are chosen. However, the E-core stator module has one more auxiliary tooth in the middle of every stator module. The auxiliary tooth influences the effective area of the air-gap flux density facing to the rotor salient poles.

Therefore, the flux through coil A can be derived as (11):

$$\begin{aligned} \varphi_A(t) &= n_{pc}\int B(\theta_s, t)ds \\ &= n_{pc} l_{stk} r_{si} \\ &\quad \times [\int_{\theta_0}^{\theta_0+\frac{\omega_{t1}}{2}} B(\theta_s, t)d\theta_s + \int_{\theta_0+\frac{\omega_{t1}}{2}+\omega_s}^{\theta_0+\frac{\omega_{t1}}{2}+\omega_s+\omega_{t_2}} \\ &\quad \times B(\theta_s, t)d\theta_s \\ &\quad + \int_{\theta_0+\frac{\omega_{t1}}{2}+\omega_s+\omega_{pm}+\omega_{t_2}}^{\theta_0+\frac{\omega_{t1}}{2}+\omega_s+\omega_{pm}+2\omega_{t_2}} B(\theta_s, t)d\theta_s \\ &\quad + \int_{\theta_0+\frac{\omega_{t1}}{2}+2\omega_s+\omega_{pm}+2\omega_{t_2}}^{\theta_0+\omega_{t_1}+2\omega_s+\omega_{pm}+2\omega_{t_2}} B(\theta_s, t)d\theta_s] \end{aligned} \tag{11}$$

where ω_{t1} and ω_{t2} denotes the width of the auxiliary tooth, the marginal tooth, respectively. To simplify the calculation the model, just supposing that $\omega_{t1} = \omega_{t2} = \omega_t$, the flux through coil A is expressed as (12), as shown at the bottom of the next page

The back-EMF is derived as (13):

$$\begin{aligned}
E_A &= \sum_{i=1,3,5}^{\infty} \left\{ \begin{array}{l} K_{A1} \cos \dfrac{p_{mo}\theta_{1\omega}}{2} \\ +K_{A2} \cos \dfrac{p_{mo}\theta_{2\omega}}{2} \end{array} \right\} \\
K_{A1} &= \mp 2 n_{pc} l_{stk} r_{si} F_i P_1 p_r \omega \cos(p_{mo}\frac{\omega_t}{2}) \cos p_{mo}\omega_{A1} \\
K_{A2} &= \mp 2 n_{pc} l_{stk} r_{si} F_i P_1 p_r \omega \cos(p_{mo}\omega_t) \cos p_{mo}\omega_{A2} \\
\omega_{A1} &= \frac{5}{4}\omega_t + \omega_{pm} + \omega_s \\
\omega_{A2} &= \frac{1}{4}\omega_t + \frac{1}{2}\omega_{pm}
\end{aligned} \tag{13}$$

The average torque can be obtained (14), as shown at the bottom of the next page,

It should be pointed that the aim is to investigate how stator module type and some critical design parameters affect the machine performance, rather than deriving an explicit mathematical expression. Thus, the PM width is assumed to be equal to the width between two modules and the width of all three teeth under one stator module is the same.

III. FINITE-ELEMENT VERIFICATION

In order to validate the foregoing analytical expressions of DSAFFSPM machines, the 12/10 U-core and 6/10 E-core DSAFFSPM machines have been designed with the same volume and same air-gap length for a fair comparison. Detailed design parameters of the two machines are listed in TABLE 1.

$$\begin{aligned}
\varphi_A(t) &= n_{pc} \int B(\theta_s, t) ds \\
&= n_{pc} l_{stk} r_{si} [\int_{\theta_0+\frac{\omega_s}{2}}^{\theta_0+\frac{\omega_s}{2}+\omega_t} B(\theta_s, t) d\theta_s \\
&\quad + \int_{\theta_0+\frac{\omega_s}{2}+\omega_{pm}+\omega_t}^{\theta_0+\frac{\omega_s}{2}+\omega_{pm}+2\omega_t} B(\theta_s, t) d\theta_s] \\
&= n_{pc} l_{stk} r_{si} \\
&\quad \times \sum_{i=1,3,5}^{\infty} \begin{array}{l} \int_{\theta_0+\frac{\omega_s}{2}}^{\theta_0+\frac{\omega_s}{2}+\omega_t} \left\{ \begin{array}{l} F_i \sin(ip_m\theta_s) \times P_0 \\ +\frac{1}{2} F_i P_1 \sin[p_{mo}\theta_s \mp p_r \omega t] \end{array} \right\} d\theta_s \\ + \int_{\theta_0+\frac{\omega_s}{2}+\omega_{pm}+\omega_t}^{\theta_0+\frac{\omega_s}{2}+\omega_{pm}+2\omega_t} \left\{ \begin{array}{l} F_i \sin(ip_m\theta_s) \times P_0 \\ +\frac{1}{2} F_i P_1 \sin[p_{mo}\theta_s \mp p_r \omega t] \end{array} \right\} d\theta_s \end{array} \\
&= -n_{pc} l_{stk} r_{si} \\
&\quad \times \sum_{i=1,3,5}^{\infty} \begin{array}{l} \{\frac{4F_iP_0}{ip_m} \cos[(ip_m)\omega_t] \sin \frac{ip_m\theta_{cons}}{2} \cos ip_m \frac{\omega_{pm}}{2} \\ +\frac{4F_iP_1}{-p_{mo}} \cos[p_{mo}\omega_t] \\ \sin \frac{p_{mo}(\theta_{cons} \mp 2p_r\omega t)}{2} \cos(p_{mo}\frac{\omega_{pm}}{2})\} \end{array} \\
\theta_{cons} &= 2\theta_0 + \omega_s + \omega_{pm} + \omega_t
\end{aligned} \tag{7}$$

$$\begin{aligned}
\varphi_A(t) &= -n_{pc} l_{stk} r_{si} \\
&\quad \times \sum_{i=1,3,5}^{\infty} \left\{ \begin{array}{l} \dfrac{4F_iP_0}{ip_m} \left[\begin{array}{l} \cos[(ip_m)\dfrac{\omega_t}{2}] \sin \dfrac{ip_m\theta_1}{2} \cos ip_m A \\ + \cos[(ip_m)\omega_t] \sin \dfrac{ip_m\theta_2}{2} \cos ip_m B \end{array} \right] \\ \dfrac{4F_iP_0}{ip_m \mp p_r} \left[\begin{array}{l} \cos(p_{mo}\dfrac{\omega_t}{2}) \sin \dfrac{p_{mo}\theta_{1\omega}}{2} \cos p_{mo} A \\ + \cos(p_{mo}\omega_t) \sin \dfrac{p_{mo}\theta_{2\omega}}{2} \cos p_{mo} B \end{array} \right] \end{array} \right\} \\
\theta_{1\omega} &= 2\theta_0 + 2\omega_s + 2\omega_{pm} + 3\omega_t \mp 2p_r\omega t \\
\theta_{2\omega} &= 2\theta_0 + 2\omega_s + 2\omega_{pm} + \frac{7}{2}\omega_t \mp 2p_r\omega t \\
A &= \frac{5\omega_t + 4\omega_{pm} + 4\omega_s}{4} \\
B &= \frac{\omega_t + 2\omega_{pm}}{4}
\end{aligned} \tag{12}$$

TABLE 1. Parameters of 12/10 U-core and 6/10 E-core AFFSPMs.

Item and symbol	12/10 U-core	6/10 E-core
Phase, m	3	
Number of stator modules, N_s	12	6
Pole number of stator-PMs, p_m	6	3
Number of rotor salient poles, p_r	10	
Pole umber of armature windings, p_a	4	7
Outside stator diameter, D_{so} (mm)	198.4	
Inside stator diameter, D_{si} (mm)	110.2	
Rotor axial length, l_r (mm)	14	
Stator axial length, l_s (mm)	25.5	
Air-gap length, g_a (mm)	1	
PM width, h_{pm} (mm)	6	

In this section, the modulation effect of rotor iron pieces will be demonstrated by showing the FEA-predicted air gap flux density waveform and their spectra of 6/10 E-core and 12/10 U-core DSAFFSPM machines.

The influence of several design parameters attached to the back-EMF and the torque, such as the ratio of teeth width to stator pole pitch (ω_t/τ_s), the ratio of PM width to stator pole pitch (ω_{pm}/τ_s) and rotor iron piece height to air-gap length(h_r/g_a), on the DSAFFSPM machines' performance, such as the flux linkage and the back-EMF, is investigated. What's more, the impact of the number of rotor salient poles is probed.

A. NO-LOAD AIR-GAP FLUX DENSITY OF 6-10 E-CORE AND 12/10 U-CORE AFFSPM

To demonstrate the flux-modulation of the modular stator U-core and E-core teeth, the open-circuit air-gap flux density and their corresponding spectrum of 6/10 E-core and 12/10 U-core DSAFFSPM machines are shown in Fig. 5 and Fig. 6. The harmonics with magnitude <0.1T are neglected to make the analysis clearer.

The air-gap flux density of 6/10 E-core DSAFFSPM machines with 3, 7, 9, 12, 13, 14, 15, 24, 26, 37 pole-pair-number working harmonics, and 12/10 U-core DSAFFSPM machines with 4, 6, 8, 16, 18, 26, 28, 30 pole-pair-number working harmonics can be shown clearly in Fig. 5(a) and Fig. 6(a). The predicted 6/10 E-core and 12/10 U-core field

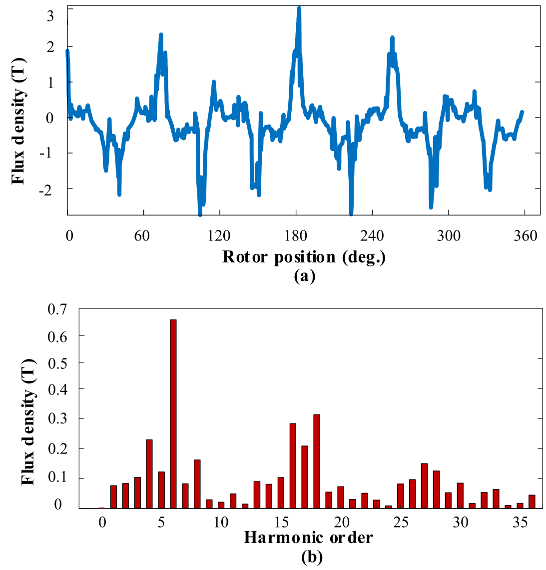

FIGURE 5. The FEA-predicted no-load air-gap flux density spectra and waveforms of 12/10 U-core DSAFFSPM machines. (a) Spectra. (b) Waveforms.

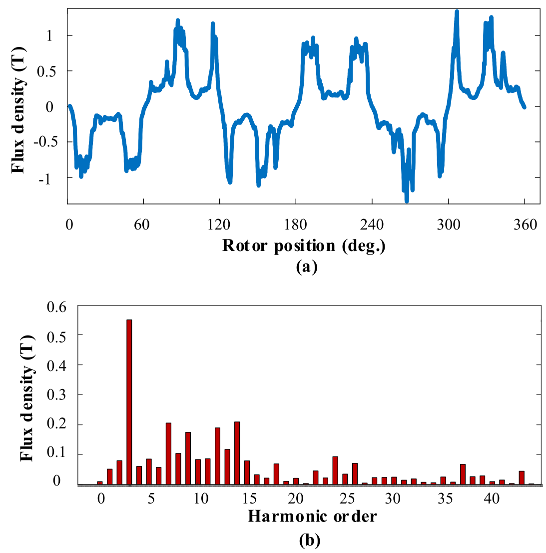

FIGURE 6. The FEA-predicted no-load air-gap flux density spectra and waveforms of 6/10 E-core DSAFFSPM machines. (a) Spectra. (b) Waveforms.

harmonics are in good agreement with the foregoing analytical (4) based on the flux modulation principle. These predicted filed harmonics can be classified into two types, 1) stationary, 2) rotating, which can be seen in Table 2.

$$
\begin{aligned}
T_e &= \left\{ \begin{aligned} & K_{T1}\cos\frac{p_{mo}(2\theta_0 + 2\omega_s + 2\omega_{pm} + 3\omega_t \mp 2p_r\omega t)}{2} \\ & +K_{T2}\cos\frac{p_{mo}(2\theta_0 + 2\omega_s + 2\omega_{pm} + \frac{7}{2}\omega_t \mp 2p_r\omega t)}{2} \end{aligned} \right\} \\
K_{T1} &= 6n_{ph}n_{pc}k_w I_A l_{stk} r_{si} F_1 P_1 p_r \omega \cos(p_{mo}\frac{\omega_t}{2}) \cos p_{mo}\omega_{A1} \\
K_{T2} &= 6n_{ph}n_{pc}k_w I_A l_{stk} r_{si} F_1 P_1 p_r \omega \cos(p_{mo}\omega_t) \cos p_{mo}\omega_{A2}
\end{aligned} \tag{14}
$$

IEEE Access

TABLE 2. Characteristics of no-load air-gap flux density harmonics.

Harmonic type	6/10 E-core	12/10 U-core
Stationary ip_m(i=1,3,5)	3, 9, 15,	6, 18, 30
Rotating $ip_m \pm kp_r$ (i=1,3,5)	7, 12, 13, 14, 24, 26, 27	4, 8, 16, 26, 28,

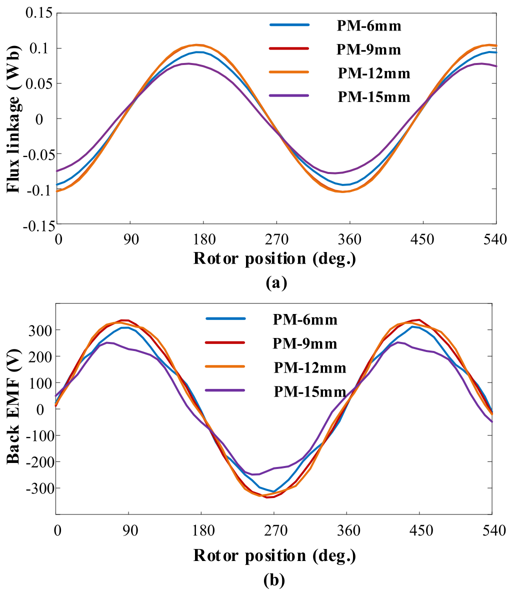

FIGURE 7. The FEA-predicted PM flux linkage and no-load back EMF waveforms of 12/10 U-core DSAFFSPM machines, with different PM widths. (a) PM flux linkage. (b) No-load back EMF.

B. PM WIDTH AND TEETH WIDTH, TO STATOR POLE PITCH

In order to discuss the influence of stator designed parameters, the flux linkage and no-load back EMF of 12/10-U-core and 6/10-E-core DSAFFSPM machines have been presented in the form of analytical formula, above in section II, and then verified using the FEA. The FEA results are displayed from Fig. 7 to Fig. 10, respectively. In order to facilitate the analysis, the stator pole pitch τ_s remains unchanged, along with the variation of PM width and teeth width.

In this case, instead of the ratio of PM width and teeth width to the stator pole pitch, the variation of PM width and teeth width can be studied. It can be seen in Fig. 7, with the width of PMs increasing, the flux linkage of the 12/10 U-core DSAFFSPM machine goes up smoothly and reaches the peak valued 0.1Wb when the width of PMs increases to 12mm. It should be noted that when PM width changes from 12mm to 15mm, the flux linkage decreases rapidly to 0.073Wb.

According to (7), the amplitude of the flux linkage is connected to the PM coefficient ω_{pms} defined in (8). when the pm width increase, the flux linkage will increase at the early stage and then decrease, which is in accordance with the FEA results. In Fig.7, the back EMF is also presented, where the trend of back EMF varying the PM width from 6mm to

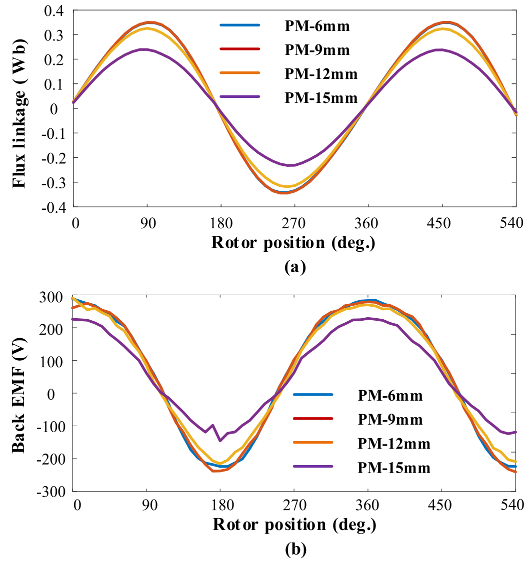

FIGURE 8. The FEA-predicted PM flux linkage and no-load back EMF waveforms of 6/10 E-core DSAFFSPM machines, with different PM widths (a) PM flux linkage. (b) No-load back EMF.

15 mm is much the same as that of flux linkage. However, compared the formula (7) with formula (8), the back EMF does not have the stationary part while the flux linkage is composed of both stationary and rotatory parts, resulting in a drop at both bottoms of the back EMF waveforms. From the aspect of magnetic path, it can be concluded that with the increase of the pm width, the circumferential PM MMF raises, and the flux density of the adjacent U-core stator iron becomes stronger. However, the permeability of the iron core remains constant, resulting in the saturation of the iron core. In the meanwhile, the flux leakage increases with the flux path going along the PM-air magnetic circuit.

Different from the U-core stator, E-core stator obtains more effective areas when the main flux returns to the stator side due to the middle teeth of the stator modular, namely auxiliary teeth. In Fig. 8(a), the flux linkage stays the same at first and then keeps dropping with the PM width increasing from 6mm to 15mm, which can be reflected in formula(12), in which the amplitude of flux linkage can be determined by both ω_{PM} and $\omega_{PM}/2$. However, in formula (7), only $\omega_{PM}/2$ is cared for the flux linkage amplitude. What's more, the sharper bottom of the negative waveform of the EMF occurs in Fig. 8(b), the reason for which is in formula (13), the superposition of two parts results in the gentle-sinusoidal-shape in positive axis part, and the steep-sinusoidal-shape in negative axis shape.

Another stator designed parameter, the width of stator teeth, should also be taken into consideration. The influence of the width of stator teeth on the flux linkage and back EMF of 12/10 U-core and 6/10 E-core DSAFFSPM machines can be also reflected in the equation (7), (8) and equation (12), (13), respectively.

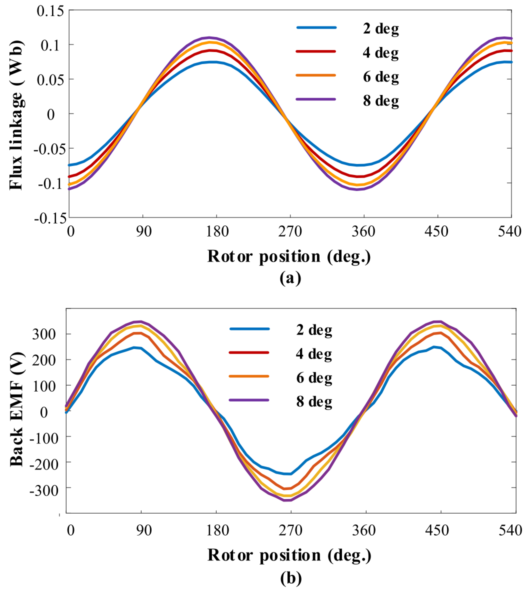

FIGURE 9. The FEA-predicted PM flux linkage and no-load back EMF waveforms of 12/10 U-core DSAFFSPM machines, with different stator tooth widths. (a) PM flux linkage. (b) No-load back EMF.

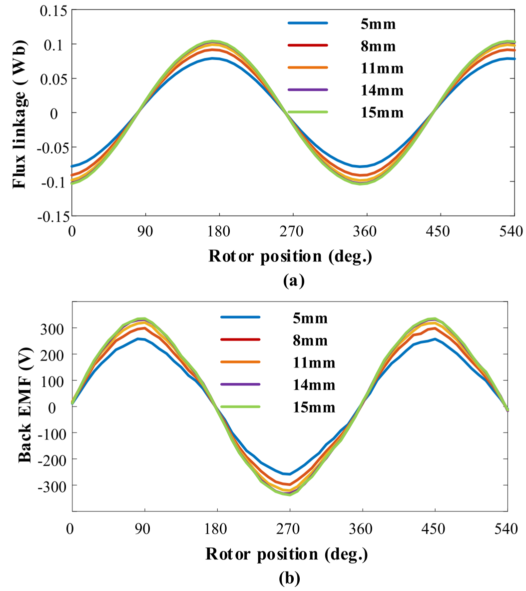

FIGURE 11. The FEA-predicted PM flux linkage and no-load back EMF waveforms of 12/10 U-core DSAFFSPM machines, with different rotor iron piece heights. (a) PM flux linkage. (b) No-load back EMF.

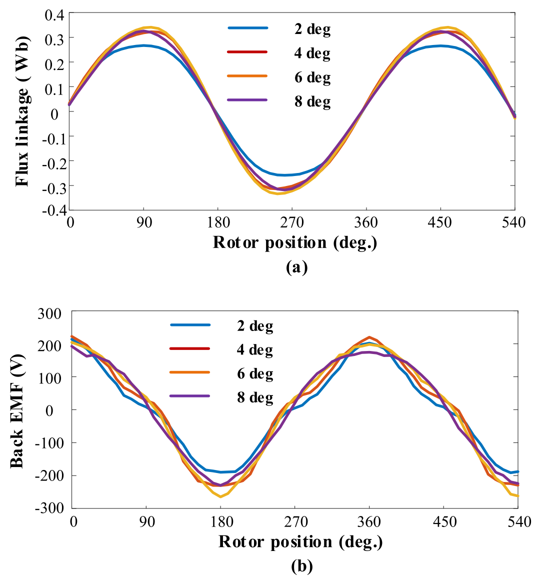

FIGURE 10. The FEA-predicted PM flux linkage and no-load back EMF waveforms of 6/10 E-core DSAFFSPM machine, with different stator tooth widths (a) PM flux linkage (b) No-load back EMF.

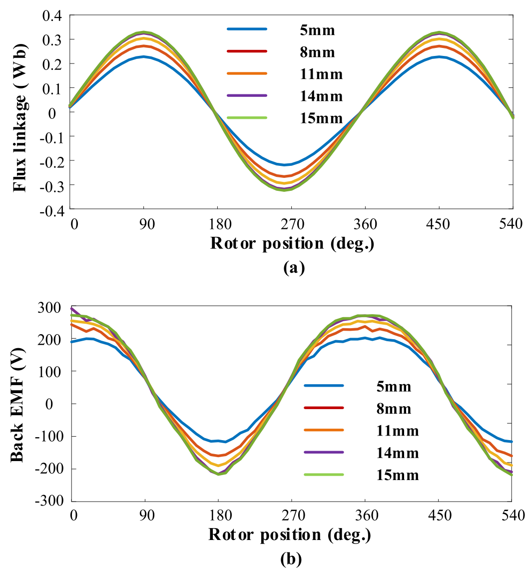

FIGURE 12. The FEA-predicted PM flux linkage and no-load back EMF waveforms of 6/10 E-core DSAFFSPM machines, with different rotor iron piece heights. (a) PM flux linkage. (b) No-load back EMF.

The FEA results are then given in Fig. 9 and Fig. 10. As shown in Fig. 9, for 12/10 U-core prototype, the increase of stator teeth width leads to the raise of the amplitudes of both flux linkage and back EMF, which is in accordance with the analytical expression. Nevertheless, for 6/10 E-core prototype, the variation of amplitude of flux linkage and back EMF is different. The flux linkage amplitude rises rapidly when stator teeth varies from 2deg to 4deg, and then keeps nearly the same with the ascendency of stator teeth. In the meanwhile, the amplitude of back EMF fluctuates with the increase of stator teeth, and the maximum back EMF occurs at stator-teeth-4deg. Comparing the formula (8) with formula(13), back EMF of 12/10 U-core prototype is only connected with ω_t while for 6/10 E-core DSAFFSPM, the parameter ω_t, $\frac{5}{4}\omega_t$, $\frac{1}{4}\omega_t$, $\frac{1}{2}\omega_t$ should all be cared.

C. ROTOR IRON PIECE HEIGHT TO AIR-GAP LENGTH (h_r/g_a)

Since the air-gap permeance can be influenced by both rotor iron height and air-gap length, the ratio of rotor iron height to air-gap length is taken into consideration. For the convenience

TABLE 3. Modulation effect of DSAFFSPM machines with different stator and rotor pole pair numbers.

p_m	p_r	p_a	G_r	Winding factor
3	10	7	1.43	0.5
	11	8	1.38	0.866
	13	10	1.3	0.866
	14	11	1.27	0.5
6	10	4	2.5	0.866
	11	5	2.2	0.933
	13	7	1.86	0.933
	14	8	1.75	0.866

TABLE 4. Characteristics of no-load air-gap flux density harmonics with different rotor poles.

Stator modular	Harmonic type	Stationary ip_m (i=1,3,5)	Rotating $ip_m \pm kp_r$ (i=1,3,5)
E-core	6/11	3, 9, 15, 21	4, 8, 14, 20, 26, 32
	6/13	3, 9, 15, 21, 39	2, 4, 10, 16, 22, 28, 29
	6/14	3, 9, 15, 21, 33, 39	11, 17, 19, 23, 25, 29
U-core	12/11	6, 18, 30	5, 7, 16, 17, 20, 29, 33
	12/13	6, 18, 30	5, 7, 19, 31
	12/14	6, 18, 30	4, 8, 16, 20, 32,36

of comparing the machine performances of different ratios, the air-gap length is set constant and is 1 mm and the rotor iron piece height varies from 5mm-18mm, which means the ratio changes from 5-18. Fig. 11 and Fig. 12 show the flux linkage and back EMF of 6/10 E-core and 12/10 U-core DSAFFSPM machines, respectively. As the height rises, the general waveform trend of both flux linkage and back EMF of these two machines is upward. Nevertheless, for 6/10 E-core prototype, when the height reaches 14 mm, the amplitude keeps still while for 12/10 U-core prototype, the height that keeps the peak value constant is 11mm. This phenomenon is mainly because that from the above analysis, the no-load air-gap flux density amplitude of 12/10 U-core prototype is higher than that of 6/10 E-core prototype, resulting in the rotor core of 6/10 E-core prototype more easily saturated. It should be noted that, Although the height-18mm waveform was not displayed in Fig. 11 and Fig. 12, both prototypes failed to operate when rotor height reaches 18mm. It can be concluded that the rotor height is so large that the magnetic circuit cannot

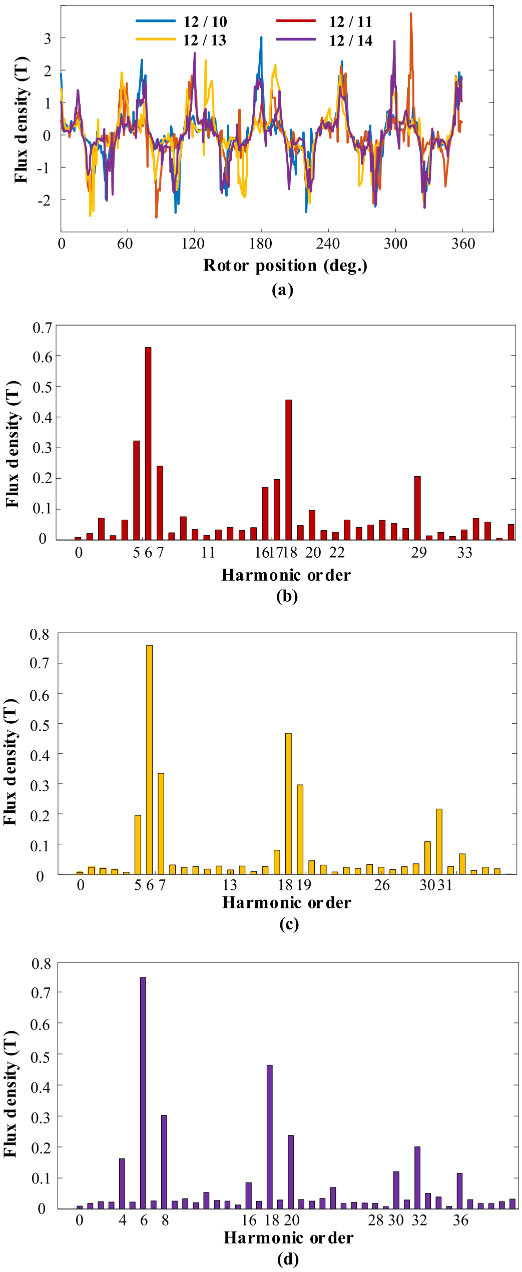

FIGURE 13. The FEA-predicted no-load air-gap flux density spectra and waveforms of 12-stator-U-core DSAFFSPM machines, with different rotor poles (a) Waveforms. (b) Spectrum of 11-rotor. (c) Spectrum of 13-rotor. (d) Spectrum of 14-rotor.

pass through the rotor to form a closed loop on both sides of the stator.

D. DIFFERENT ROTOR POLE NUMBERS

In this section, the modulation principle in both 12-stator-U-core-modular and 6-stator-E-core-modular DSAFFSPM machines having 11, 13, 14 rotor poles are analyzed.

Table 3 demonstrates the modulation effect of AFFSPMs and present a concept of gear ratio G_r given by formula (15), which can be used to characterize the torque capability [28].

$$G_r = \frac{p_r}{p_a} \tag{15}$$

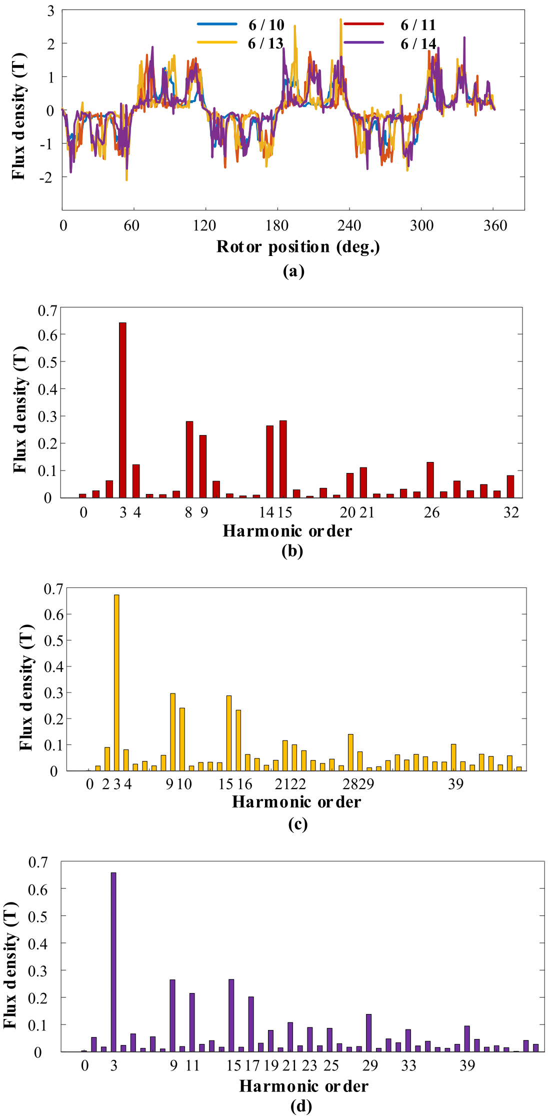

FIGURE 14. The FEA-predicted no-load air-gap flux density waveforms and corresponding spectra of 6-stator-E-core DSAFFSPM machines, with different rotor poles. (a) Waveforms. (b) Spectrum of 11-rotor. (c) Spectrum of 13-rotor. (d) Spectrum of 14-rotor.

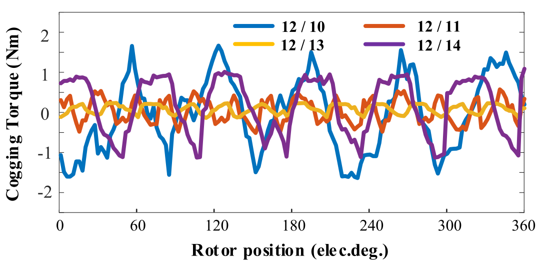

FIGURE 15. The FEA-predicted cogging torque waveforms of 12-stator-U-core DSAFFSPM machines with different rotor poles.

$$p_a = p_r - p_m \tag{16}$$

Since the concentrated windings are adopted in DSAFFSPM machines to shorten the end of winding, the winding factor of different stator-rotor-pole combinations is also presented. In general, the gear ratio, as well as the winding factor of 6-stator-E-core-modular-DSAFFSPM machines is higher than that of 12-stator-U-core-modular-DSAFFSPM machines. On the other hand, the winding factor of even-rotor-pole-pair-number often exceeds that of odd-rotor-pole-pair-number. Therefore, a proper stator/rotor-pole combination can be chosen to make a balance between a high gear ratio and high winding factor based on the above analysis.

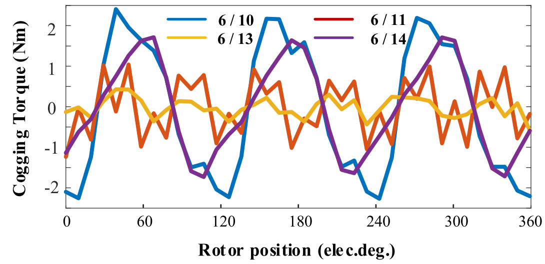

FIGURE 16. The FEA-predicted cogging torque waveforms of 6-stator-E-core DSAFFSPM machines with different rotor poles.

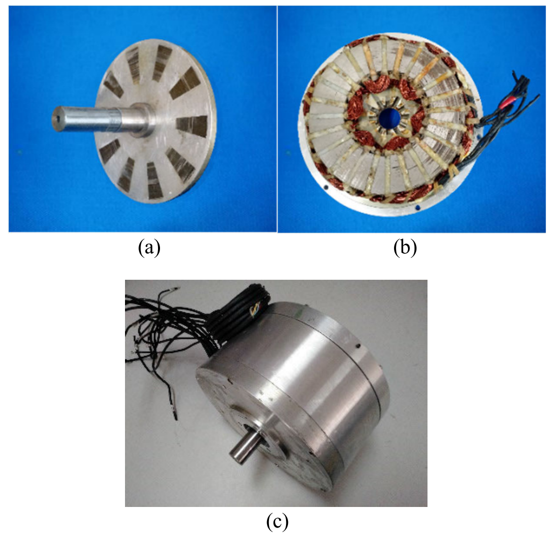

FIGURE 17. Pictures of a 12/10 U-core DSAFFSPM machine. (a) 10-pole rotor. (b) Stator with 12 U-core modules. (c) Prototype machine.

The predicted cogging torque waveforms with different rotor poles are compared in Fig. 15 and Fig. 16, where it can be seen that the 12-stator DSAFFSPM machines has smaller cogging torque than 6-stator DSAFFSPM machines. On the other hand, the cogging torque amplitude of machines with odd-pole-pair-number-rotor often surpasses that of machines with even-pole-pair-number-rotor. Obviously, in the same electrical period, the former machines have more cogging torque periods than the latter machines, which is closely connected to the least common multiple of stator poles and rotor poles.

The no-load flux density and corresponding spectrum of 12/11, 12/13, 12/14 U-core and 6/10, 6/11, 6/13, 6/14 E-core are compared in Fig. 13 and Fig. 14, whose dominating flux density harmonics of these machines are collected in Table 4. To make the analysis clearer, only amplitudes

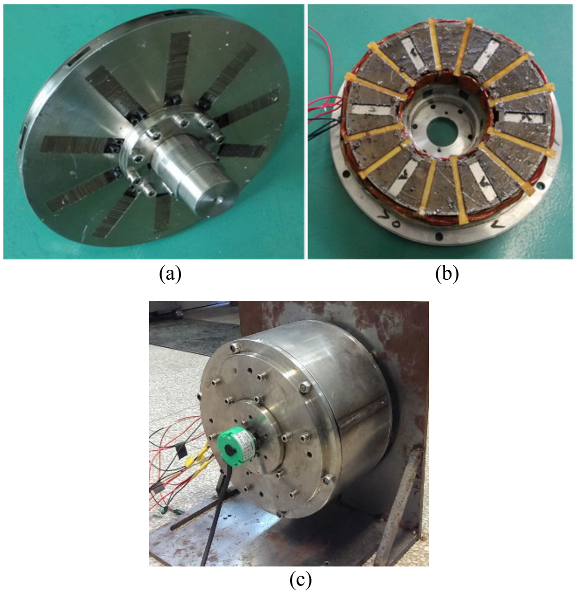

FIGURE 18. Pictures of a 6/10 E-core DSAFFSPM machine. (a) 10-pole rotor. (b) Stator with 6 E-core modules. (c) Prototype machine.

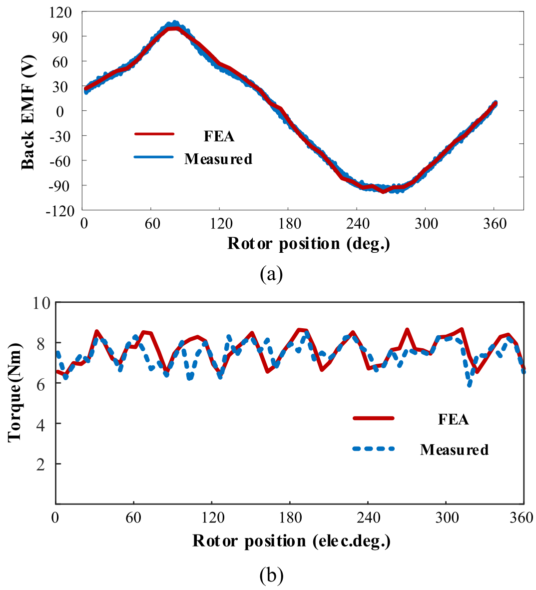

FIGURE 19. Comparison of measured and predicted waveforms of the 12/10 U-core DSAFFSPM machine. (a) Back EMF. (b) Torque.

of the flux density over 0.1T are chosen. From Table 4, in terms of stationary harmonics, the dominant harmonic of DSAFFSPM machines with same number of stator poles is approximately the same, while for rotating harmonics, the dominating harmonics of DSAFFSPM machines with odd-rotor-pole-pair-number are different from that with even-rotor-pole-pair-number.

IV. EXPERIMENTAL RESULTS

In order to validate the above analysis, a 12/10 U-core DSAFFSPM machine and a 6/10 E-core DSAFFSPM machine are prototyped. Their stator, rotor and whole structure photos are displayed in Fig. 17 and Fig. 18, respectively. The no-load flux density and its corresponding spectrum based on flux modulation in the above sections cannot be tested directly in the prototyped machines, only the back-EMF and electromagnetic torque can be shown in the experimental results.

Firstly, the line-line back EMF is tested and compared with the FEA result in Fig. 19(a) and Fig. 20(a). It can be seen that the FEA predicted results are in good agreements with the measured waveforms. Fig. 19(b) and Fig. 20(b) show the electromagnetic torque waveforms predicted by FEA and tested by experiment, and two curves match well.

Finally, the key different parameters, such as the average torque and efficiency of 6/10 and 12/10 DSAFFSPM machines are presented in Table 5.

TABLE 5. Performance comparison of 6/10 and 12/10 DSAFFSPM machines.

Parameters	12/10 U-core	6/10 E-core
Average torque	7.78N.m	5.41N.m
Torque density	48kN/m^3	55kN/m^3
Efficiency	0.74	0.86
Speed	750r/min	3000r/min

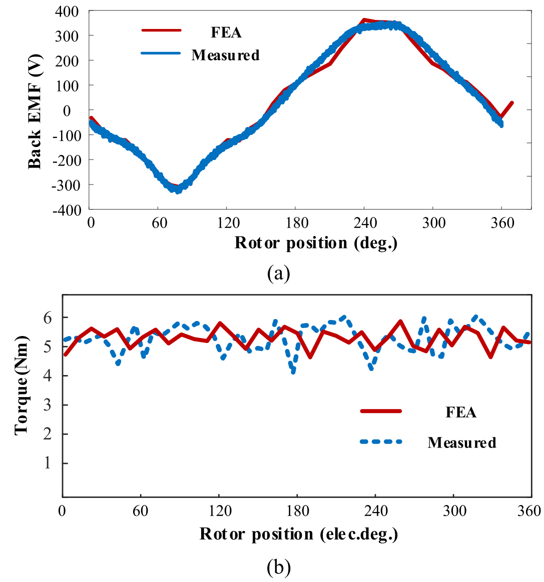

FIGURE 20. Comparison of measured and predicted waveforms of the 6/10 E-core DSAFFSPM machine. (a) Back EMF. (b) Torque.

V. CONCLUSION

In this paper, dual-stator axial-field flux-switching permanent magnet (DSAFFSPM) motors with E-core and U-core stator modular segments, as well as different rotor poles are compared based on flux modulation principle. The analytical expressions of no-load flux density, flux linkage, back EMF and the electromagnetic torque are derived, using a MMF-permeance-model, with consideration of stator and rotor designed parameters, such as PM width, stator teeth width and rotor height.

Specially, the 6/10 E-core DSAFFSPM machines are more likely to be influenced by stator designed parameters since there are several parts contributing to the formula of the back EMF and the electromagnetic torque, and its rules can be seen clearly. Also, the impact of different rotor poles on gear ratio, winding factor and no-load flux density is investigated. 12-stator U-core DSAFFSPM machines obtain a higher winding factor and gear ratio. However, the 6-stator E-core possess a better torque density. In terms of the cogging torque, 6-stator E-core DSAFFSPM machines often have larger cogging torque than 12-stator U-core DSAFFSPM machines and machines with odd-pole-pair-number-rotor have smaller cogging torque, such as 6/11, 6/13, 12/11, 12/13 DSAFFSPM machines. Benefiting from the above analysis, a proper stator-rotor slot/pole combination and appropriate stator and rotor size can be selected with corresponding performance requirements such as the winding factor and the gear ratio.

REFERENCES

[1] H. Zhou, W. Tao, C. Zhou, Y. Mao, G.-J. Li, and G. Liu, "Consequent pole permanent magnet Vernier machine with asymmetric air-gap field distribution," *IEEE Access*, vol. 7, pp. 109340–109348, Aug. 2019.

[2] Y. Kong, M. Lin, and L. Jia, "A novel high power density permanent-magnet synchronous machine with wide speed range," *IEEE Trans. Magn.*, vol. 56, no. 2, pp. 1–6, Feb. 2020.

[3] L. Jia, M. Lin, W. Le, N. Li, and Y. Kong, "Dual-skew magnet for cogging torque minimization of axial flux PMSM with segmented stator," *IEEE Trans. Magn.*, vol. 56, no. 2, pp. 1–6, Feb. 2020.

[4] N. Li, J. Zhu, M. Lin, G. Yang, Y. Kong, and L. Hao, "Analysis of axial field flux-switching memory machine based on 3-D magnetic equivalent circuit network considering magnetic hysteresis," *IEEE Trans. Magn.*, vol. 55, no. 6, pp. 1–4, Jun. 2019.

[5] D. Xu, M. Lin, X. Fu, L. Hao, W. Zhang, and N. Li, "Cogging torque reduction of a hybrid axial field flux-switching permanent-magnet machine with three methods," *IEEE Trans. Appl. Supercond.*, vol. 26, no. 4, pp. 1–5, Jun. 2016.

[6] H. Li, Z. Q. Zhu, and H. Hua, "Comparative analysis of flux reversal permanent magnet machines with toroidal and concentrated windings," *IEEE Trans. Ind. Electron.*, vol. 67, no. 7, pp. 5278–5290, Jul. 2020.

[7] S. Niu, X. Zhao, X. Zhang, and T. Sheng, "A novel axial-flux-complementary doubly salient machine with boosted PM utilization for cost-effective direct-drive applications," *IEEE Access*, vol. 7, pp. 145970–145977, Oct. 2019.

[8] S. E. Rauch and L. J. Johnson, "Design principles of flux-switch alternators [includes discussion]," *Trans. Amer. Inst. Electr. Eng. III: Power App. Syst.*, vol. 74, no. 3, pp. 1261–1268, Jan. 1955.

[9] R. Cao, C. Mi, and M. Cheng, "Quantitative comparison of flux-switching permanent-magnet motors with interior permanent magnet motor for EV, HEV, and PHEV applications," *IEEE Trans. Magn.*, vol. 48, no. 8, pp. 2374–2384, Aug. 2012.

[10] A. Fasolo, L. Alberti, and N. Bianchi, "Performance comparison between switching-flux and IPM machines with rare-Earth and ferrite PMs," *IEEE Trans. Ind. Appl.*, vol. 50, no. 6, pp. 3708–3716, Nov. 2014.

[11] A. S. Thomas, G. W. Jewell, and Z. Q. Zhu, "Comparison of flux switching and surface mounted permanent magnet generators for aerospace applications," in *Proc. 5th IET Int. Conf. Power Electron., Mach. Drives (PEMD)*, Brighton, U.K., 2010, pp. 1–5.

[12] Z. Q. Zhu and J. T. Chen, "Advanced flux-switching permanent magnet brushless machines," *IEEE Trans. Magn.*, vol. 46, no. 6, pp. 1447–1453, Jun. 2010.

[13] Z. Z. Wu and Z. Q. Zhu, "Analysis of air-gap field modulation and magnetic gearing effects in switched flux permanent magnet machines," *IEEE Trans. Magn.*, vol. 51, no. 5, pp. 1–12, May 2015.

[14] W. Zhang, X. Liang, and M. Lin, "Analysis and comparison of axial field flux-switching permanent magnet machines with three different stator cores," *IEEE Trans. Appl. Supercond.*, vol. 26, no. 7, pp. 1–6, Oct. 2016.

[15] Y. Yao and Q. Lu, "Comparative study of E-core and C-core modular PM linear machines with different slot/pole combinations," *IEEE Trans. Magn.*, vol. 53, no. 11, pp. 1–7, Nov. 2017.

[16] W. Zhao, T. A. Lipo, and B.-I. Kwon, "A novel dual-rotor, axial field, fault-tolerant flux-switching permanent magnet machine with high-torque performance," *IEEE Trans. Magn.*, vol. 51, no. 11, pp. 1–4, Nov. 2015.

[17] W. Zhao, T. A. Lipo, and B.-I. Kwon, "Comparative study on novel dual stator radial flux and axial flux permanent magnet motors with ferrite magnets for traction application," *IEEE Trans. Magn.*, vol. 50, no. 11, pp. 1–4, Nov. 2014.

[18] W. Jiang, W. Huang, X. Lin, Y. Zhao, and S. Zhu, "Analysis of rotor poles and armature winding configurations combinations of wound field flux switching machines," *IEEE Trans. Ind. Electron.*, early access, Jul. 21, 2020, doi: 10.1109/TIE.2020.3009578.

[19] J. Yu, C. Liu, Z. Song, and H. Zhao, "Permeance and inductance modeling of a double-stator hybrid-excited flux-switching permanent-magnet machine," *IEEE Trans. Transp. Electrific.*, vol. 6, no. 3, pp. 1134–1145, Sep. 2020.

[20] J. Zhu, L. Wu, W. Zheng, Q. Zhou, and T. Li, "Magnetic circuit modeling of dual-armature flux-switching permanent magnet machine," *IEEE Trans. Magn.*, vol. 57, no. 1, pp. 1–13, Jan. 2021, doi: 10.1109/TMAG.2020.3035280.

[21] A. Mohammadi Ajamloo, A. Ghaheri, H. Shirzad, and E. Afjei, "Non-linear analytical modelling and optimisation of a 12/8 rotor excited flux-switching machine," *IET Electr. Power Appl.*, vol. 14, no. 9, pp. 1592–1603, Sep. 2020.

[22] Y. Zhou and X. Wu, "Analytical calculation of magnetic field of bearing-less flux-switching permanent-magnet machine based on doubly-salient relative permeance method," *IET Electr. Power Appl.*, vol. 14, no. 5, pp. 872–884, May 2020.

[23] M. Lin, L. Hao, X. Li, X. Zhao, and Z. Q. Zhu, "A novel axial field flux-switching permanent magnet wind power generator," *IEEE Trans. Magn.*, vol. 47, no. 10, pp. 4457–4460, Oct. 2011.

[24] L. Hao, M. Lin, D. Xu, X. Fu, and W. Zhang, "Static characteristics of a novel axial field flux-switching permanent magnet motor with three stator structures," *IEEE Trans. Magn.*, vol. 50, no. 1, pp. 1–4, Jan. 2014.

[25] J.-W. Kwon, N. Baloch, and B.-I. Kwon, "High gear ratio flux switching permanent magnet machine for high torque performance," *IEEE Access*, vol. 8, pp. 121630–121636, 2020.

[26] H. Li, Z. Q. Zhu, and Y. Liu, "Optimal number of flux modulation pole in Vernier permanent magnet synchronous machines," *IEEE Trans. Ind. Appl.*, vol. 55, no. 6, pp. 5747–5757, Nov. 2019.

[27] J. T. Chen, Z. Q. Zhu, S. Iwasaki, and R. P. Deodhar, "A novel E-core switched-flux PM brushless AC machine," *IEEE Trans. Ind. Appl.*, vol. 47, no. 3, pp. 1273–1282, May 2011.

[28] T. Zou, D. Li, R. Qu, and D. Jiang, "Performance comparison of surface and spoke-type flux-modulation machines with different pole ratios," *IEEE Trans. Magn.*, vol. 53, no. 6, pp. 1–5, Jun. 2017.

SHUAI WANG was born in 1996. He received the B.S. degree in electrical engineering from the Shenyang University of Technology, Shenyang, China, in 2014. He is currently pursuing the Ph.D. degree with Southeast University.

His current research interest includes the design and optimization of the axial-field magnetic-geared machines.

KEMAN LIN (Member, IEEE) was born in Nanjing, China, in 1987. She received the B.S. and Ph.D. degrees in electrical engineering from Southeast University, Nanjing, in 2010 and 2016, respectively.

She is currently an Assistant Professor of electrical engineering with Hohai University, Nanjing. Her current research interests include modeling and control of renewable energy generation, electric machines, and power system stability analysis.

MINGYAO LIN (Member, IEEE) received the B.S., M.S., and Ph.D. degrees in electrical engineering from Southeast University, Nanjing, China, in 1982, 1985, and 1995, respectively.

In 1985, he joined the School of Electrical Engineering, Southeast University, where he has been a Professor of electrical machines and control systems, since 2004. In 2002, he was a Visiting Scholar with the Esslingen University of Applied Sciences, Esslingen, Germany.

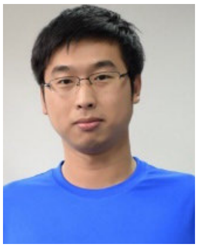

YONG KONG received the bachelor's degree in electrical and automation engineering from Shandong Jianzhu University, Jinan, China, in 2013. He is currently pursuing the Ph.D. degree in electric motors and drives with Southeast University, Nanjing, China. From July 2019 to July 2020, he was a joint Ph.D. Student funded by the China Scholarship Council with the Department of Electrical Engineering, University of Padova, Padova, Italy, where he focused on the efficiency analysis and optimization of the electric machines in electric vehicles.

DA XU was born in 1989. She received the Ph.D. degree in electrical engineering from Southeast University, Nanjing, China, in 2017. Since 2017, she has been with the Nanjing University of Science and Technology, as a Lecturer. Her current major research interest includes the design, analysis, and control of the hybrid axial field flux-switching permanent magnet machine for automotive applications.

NIAN LI received the B.E. degree in electrical engineering and automation from the Nanjing University of Science and Technology, Nanjing, China, in 2012, and the Ph.D. degree in electrical engineering from Southeast University, Nanjing, in 2019.

In 2019, he joined the School of Automation, Nanjing University of Science and Technology. His current research interests include numerical methods and design and analysis of novel permanent magnet machines, in particular permanent magnet memory machines.

PENG WANG received the B.S. degree in electrical engineering from the Nanjing Institute of Technology, Nanjing, China, in 2018. He is currently pursuing the M.S. degree in electrical engineering with Southeast University, Nanjing.

His current research interests include sensorless control and online parameters estimation for motor drivers.